

submitted to ApJ

Extrinsic Radio Variability of JVAS/CLASS Gravitational Lenses

L.V.E. Koopmans

*Space Telescope Science Institute, 3700 San Martin Drive, Baltimore, MD 21218
 California Institute of Technology, Theoretical Astrophysics, 130-33, Pasadena, CA 91125
 Jodrell Bank Observatory, Macclesfield, Cheshire, SK11 9DL, UK*

koopmans@stsci.edu

A. Biggs

*Joint Institute for VLBI in Europe, P.O. Box 2, 7990 AA, Dwingeloo, The Netherlands
 Jodrell Bank Observatory, Macclesfield, Cheshire, SK11 9DL, UK*

R.D. Blandford

California Institute of Technology, Theoretical Astrophysics, 130-33, Pasadena, CA 91125

I.W.A. Browne, N.J. Jackson, S. Mao, P.N. Wilkinson

Jodrell Bank Observatory, Macclesfield, Cheshire, SK11 9DL, UK

A.G. de Bruyn

*ASTRON, P.O. Box 2, 7990 AA, Dwingeloo, The Netherlands
 Kapteyn Astronomical Institute, P.O. Box 800, 9700 AV Groningen, The Netherlands*

J. Wambsganss

Universität Potsdam, Institut für Physik, Am Neuen Palais 10, 14469 Potsdam, Germany

ABSTRACT

We present flux-ratio curves of the *fold* and *cusp* (i.e. close multiple) images of six JVAS/CLASS gravitational lens systems. The data were obtained over a period of 8.5 months in 2001 with the Multi-Element Radio-Linked Interferometer Network (MERLIN) at 5-GHz with 50 mas resolution, as part of a MERLIN Key-Project. Even though the time delays between the fold and cusp images are small ($\lesssim 1$ d) compared to the time-scale of intrinsic source variability, all six

lens systems show evidence that suggests the presence of extrinsic variability. In particular, the cusp images of B2045+265 – regarded as the strongest case of the violation of the cusp relation (i.e. the sum of the magnifications of the three cusp images add to zero) – show extrinsic variations in their flux-ratios up to $\sim 40\%$ peak-to-peak on time scales of several months. Its low Galactic latitude of $b \approx -10^\circ$ and a line-of-sight toward the Cygnus superbubble region suggest that Galactic scintillation is the most likely cause. The cusp images of B1422+231 at $b \approx +69^\circ$ do not show strong extrinsic variability. Galactic scintillation can therefore cause significant scatter in the cusp and fold relations of some radio lens systems (up to 10% rms), even though these relations remain violated when averaged over a $\lesssim 1$ year time baseline.

Subject headings: gravitational lensing — scattering — ISM: general

1. Introduction

Cosmological Cold–Dark–Matter (CDM) simulations predict the existence of condensed structures in the halos around massive galaxies (e.g. Klypin et al. 1999; Moore et al. 1999), if the initial power-spectrum does not cut off at small scales and dark matter is cold and not self-interacting. However, observationally, we see at most the high-mass tail of these structures in the form of dwarf galaxies. This raises the question of where most of their less massive ($10^6 - 10^9 M_\odot$) counterparts are located. Either (i) these CDM structures have not formed – in conflict with CDM predictions – or (ii) they consist predominantly of dark-matter and baryons have been blown out, preventing star formation altogether, or (iii) baryons are present but have not condensed inside their potential well to form visible stars. If either one of the latter two is the case, the only way to detect them is through their gravitational effect, in particular through dynamics and lensing.

The initial suggestion by Mao & Schneider (1998) that anomalous flux-ratios in the lens system B1422+231 can be caused by small-scale mass substructure in the lens galaxy, was recently extended to a larger – although still limited – sample of gravitational-lens systems with fold and cusp images (Metcalf & Madau 2001; Keeton 2001; Chiba 2002; Metcalf & Zhao 2002; Dalal & Kochanek 2002; Bradač et al. 2002; Keeton et al. 2002). In particular, analyses have focused on the so called normalized “cusp relation”, which says that $R_{\text{cusp}} \equiv \Sigma \mu_i / \Sigma |\mu_i| \rightarrow 0$, for the magnifications μ_i of the three merging images of a source well inside the cusp (Blandford 1990; Schneider & Weiss 1992). A similar relation holds for the two fold images. These relations are only two of many (in fact ∞) scaling laws (Blandford 1990). Because globular clusters and dwarf-galaxies are too few in number

to explain the rate of anomalous flux-ratios and cusp relations, this could be used as an argument in favor of CDM substructure as the dominant cause of these apparent anomalies (e.g. Kochanek & Dalal 2003).

If the observed violations of the cusp relation (i.e. $R_{\text{cusp}} \neq 0$), as discussed above, are due to substructure on mass scales of 10^6 to 10^9 M_{\odot} , the effect should be the same for radio and optical flux ratios (if the latter are available), and it should be constant in time. However, another possible explanation is microlensing of stellar mass objects in combination with a smoothly distributed (dark) matter component (Schechter & Wambsganss 2002). This one does not require the optical and radio flux ratios to behave in the same way, and in particular it predicts the optical flux ratios to *change* over time scales of years. Finally, there is also the possibility that the flux-density and surface brightness distribution of lensed radio images are affected by the ionized ISM in the lens galaxy and/or our Galaxy, also leading to changes in the apparent value of the cusp relation.

Hence, before one can confidently accept the detection CDM substructure, it requires rigorous testing to see whether observed flux ratios correspond to magnification ratios or whether they can be affected by propagation effects (or microlensing). Here, we make the first coordinated attempt to test the effects of propagation on the observed *radio* fluxes of lensed images.

In Sections 2 and 3 we present the first results of our MERLIN Key-Project (Biggs et al. 2003) to search for extrinsic variability between fold and cusp images (i.e. close multiple images), based on their flux-density curves. A discussion and conclusions are given in Sect.4.

2. MERLIN 5-GHz Data

MERLIN 5-GHz data were obtained between Feb 21 and Nov 7 2001. A total of 41 epochs of 24 hours each were obtained, on average once per week. Eight lens systems were observed (i.e. Table 1 plus B1608+656 and B1600+434) of which seven are four-image systems and one is a double. The data acquisition and reduction is described in Biggs et al. (2003), which also presents the flux-density curves of all the lensed images.

In this paper, we focus on the *flux-ratio* curves. This approach has several advantages when looking for extrinsic variability. The dominant errors on flux-density curves in the radio are those resulting from residual noise in the maps and from multiplicative errors as a result of erroneous flux calibration. Because multiplicative errors are equal for each of the lensed images, they disappear in the flux-ratio curves (not corrected for the time-delays) which should therefore be flat and dominated by noise in the absence of variability.

All presented lens systems also have small time-delays between cusp/fold images ($\lesssim 1$ d) compared to the time between observations and the time-scale of intrinsic variability as seen in the flux-density curves (Biggs et al. 2003). Hence, intrinsic flux-density variations should effectively occur simultaneously in fold and cusp images and thus disappear in the flux-ratio curves. Throughout this paper we therefore assume that (i) due to the small time-delays between fold/cusp images, intrinsic variability does not affect the flux-ratio curves, (ii) systematic flux-density errors are multiplicative and also do not affect the flux-ratio curves, and (iii) extrinsic variability does not correlate between lensed images.

We exclude the double B1600+434 and the quad B1608+656 from our analysis, which both have non-negligible time-delays (i.e. several weeks to months; see Fassnacht et al. 1999a, 2002; Koopmans et al. 2000; Burud et al. 2000).

3. Results

3.1. Normalized Flux-ratio Curves

In Fig.1 the resulting flux-ratio curves of all images are shown with respect to image A which is often the brightest image. We follow the labeling of these images as published in the literature (e.g. Biggs et al. 2003). Each flux-ratio curve has been normalized to unity by dividing them through the average flux-ratio of all 41 epochs. The errors are the square root of the sum of the two fractional (noise) errors on the flux-densities squared. The flux-density errors are determined from the rms in the residual maps (i.e. the radio maps with the lensed images subtracted).

In Table 1, we list (i) the average flux-ratios and the rms scatter for each image pair, (ii) the reduced- χ^2 values, by assuming that each normalized flux-ratio should be unity in the case of no extrinsic variability and under the assumptions mentioned in Sect.2, and (iii) the values of R_{cusp} (see Mao & Schneider 1998; Keeton et al. 2002), which we discuss further in Sect.4.

3.2. Evidence for Extrinsic Variability

To test for extrinsic variability in the lensed images, on time-scales less than the monitoring period of 8.5 month, we introduce the following method:

Let us designate the normalized light curves of the individual cusp/fold images as $a_n \equiv A/\langle A \rangle$, $b_n \equiv B/\langle B \rangle$ and $c_n \equiv C/\langle C \rangle$, where their average flux-densities over the 41 epochs

are $\langle A \rangle$, $\langle B \rangle$ and $\langle C \rangle$, respectively¹

First, the points (a_n, b_n, c_n) are plotted in a three-dimensional Cartesian space, such that multiplicative errors and intrinsic flux-density variations (the latter because of the negligible time-delays) move points parallel to the vector $(1, 1, 1)$.

Second, each point (a_n, b_n, c_n) is projected on to a two-dimensional plane that is normal to the vector $(1, 1, 1)$. Hence, the projected points will *not* move on that plane, either because of intrinsic flux-density variations or multiplicative errors. Both of these are movements perpendicular to the plane and thus translate to the same projected point.

Third, if one defines the x -axis, \hat{x} , of this two-dimensional plane to be the projected a -axis, \hat{a} , of the three-dimensional space, and \hat{y} to be perpendicular to \hat{x} in the same normal plane, one finds the following simple mapping:

$$\begin{aligned} x &= (2a_n - b_n - c_n)/\sqrt{6} \\ y &= (b_n - c_n)/\sqrt{2} \end{aligned} \quad (1)$$

or in polar coordinates

$$\begin{aligned} r^2 &= x^2 + y^2 \\ \theta &= \arctan(x, y). \end{aligned} \quad (2)$$

Because \hat{a} projects on to \hat{x} , any uncorrelated extrinsic variations in image A will only result in a movement of a point along \hat{a} and thus only along the \hat{x} axis.

Because the $1-\sigma$ errors on the normalized flux-densities a_n , b_n and c_n are known from the observations, one can calculate the corresponding expected $1-\sigma$ errors on x and y .

$$\begin{aligned} \sigma_x^2 &= 2/3 \sigma_a^2 + 1/6 \sigma_b^2 + 1/6 \sigma_c^2 \\ \sigma_y^2 &= 1/2 \sigma_b^2 + 1/2 \sigma_c^2 \end{aligned} \quad (3)$$

and similarly

$$\sigma_r^2 = ((2a_n - b_n - c_n)^2 \sigma_a^2 + (2b_n - c_n - a_n)^2 \sigma_b^2 + (2c_n - a_n - b_n)^2 \sigma_c^2)/(9r^2). \quad (4)$$

Notice that the scatter in x will be a combination of the scatter in a_n , b_n and c_n , if each image behaves independently.

¹We use the notation A , B , C and a_n , b_n , c_n to indicate both the light curves as a whole, as well as their individual flux-density values.

On the other hand,

$$\chi_r^2 = \frac{1}{\text{DOF}} \sum_i (r_i/\sigma_{r,i})^2 \quad (5)$$

is a direct estimator of the significance of the presence of extrinsic variability on time-scales of <8.5 month, *irrespective of the image(s) it occurs in*. In other words, it does not tell us which image or images exhibit extrinsic variability, only that extrinsic variability is present if χ_r^2 is significantly larger than unity.

The significance of extrinsic variability in individual image is far more difficult to assess. However, we can estimate the level of extrinsic variability in image A, for example, by knowing that the expected variance in that image, due to noise *and* in the absence of extrinsic variability, should be

$$E\{\langle \sigma_a^2 \rangle\} \approx 3/2 \text{var}(x) - 1/2 \text{var}(y). \quad (6)$$

If the observed value of $\langle \sigma_a^2 \rangle = (\sum_i^N \sigma_{a,i}^2)/N$ is smaller than $E\{\langle \sigma_a^2 \rangle\}$, the difference is due to extrinsic variability with an estimated variance of

$$\text{var}(a_{\text{ext}}) \approx E\{\langle \sigma_a^2 \rangle\} - \langle \sigma_a^2 \rangle. \quad (7)$$

The same procedure can be repeated for each of the other images. In Table 2, we have listed the values of χ_r^2 and the values of $\text{var}(a_{\text{ext}}, b_{\text{ext}}, c_{\text{ext}})$, if larger than zero (note that $E\{\langle \sigma_a^2 \rangle\}$ is an estimate and could therefore be smaller than $\langle \sigma_a^2 \rangle$ when measured from a finite set of observations).

Finally, we further discuss whether correlations between the flux measurements of the merging images could potentially occur. We note, however, that $\sigma_{a/b/c}$ are noise errors as determined from residual maps, i.e. the original maps after we subtract of the best-fit model of the lensed images. The residual radio maps are consistent with noise maps. Since the images are separated by many beam sizes (i.e. resolution elements), the flux measurements of images A, B and C – even though measured from the same map – are independent, except for the multiplicative errors as explained previously. Hence there should be *no* effect of measurement correlations in Eq.(3) or (4), which could skew our results.

Hence, the technique discussed above is explicitly designed to separate the effects of multiplicative errors, extrinsic variability and noise, and should also be free of measurement correlations. For example, if one were to cross correlate (e.g. using the Spearman rank correlation) the flux-ratio curves (Fig.1) of a single lens system with each other, one would find that they correlate strongly, even in the absence of extrinsic variability. The reason being that the same noise variations in image A would be introduced in both $(B/A)_n$ and $(C/A)_n$. A Spearman rank correlation on flux-ratio curves without extrinsic variability but with similar noise properties and number of epochs confirms this. However, one notices from

equations 3 and 4 that any multiplicative error does not affect $\sigma_{x/y}^2$ or σ_r^2 (where it cancels out) or the projection on the plane that we defined in equations 1 and 2, as previously discussed. In addition, one finds from equations 1, 2 and 4 that if there is no extrinsic variability, $\chi_r^2 \rightarrow 1$, whereas the presence of extrinsic variability implies $\chi_r^2 > 1$. Hence, χ_r^2 is indeed independent from multiplicative errors and therefore the correct estimator of the significance of the presence of extrinsic variability, in the (shown) absence of measurement correlations.

3.3. Individual Lens Systems

Here, we discuss each case, based on their reduced χ^2 values. Image D is not considered because of its faintness and larger inferred time-delay compared with the other images.

3.3.1. All systems, except B2045+265

Based on the relatively low values of χ_r^2 and the estimated levels of extrinsic variability (Table 2) for the images of B0128+437, B1359+154 and B1422+231 and B1555+375, and the remaining possibility that some minor undetected additive errors could be present, the evidence for extrinsic variability in these four systems is not totally convincing. We exclude these from further discussion.

In the case of B0712+472, the reduced χ^2 values of the $(B/A)_n$ flux-ratio curves and also χ_r^2 seem more significant. In Fig.1 we see that a large number of epochs are deviant over the entire observing season. Deviations of the $(C/A)_n$ flux-ratio curve from unity are less significant, probably because image C has a larger fractional error than images A and B. Even though there is some evidence in this system for extrinsic variability between the two fold images, we conservatively regard it also as weak and we will concentrate our discussion on B2045+265. In Sect.4, however, we further discuss what a possible reason for some of the higher values of χ_r^2 and extrinsic variability can be.

3.3.2. B2045+265

In Tables 1 and 2, we see that (i) both the $(B/A)_n$ and $(C/A)_n$ flux-ratio curves have very high values of the reduced χ^2 , reflected also in large rms values, (ii) the estimated rms values of extrinsic variability and the value of χ_r^2 are very large, and (iii) a visual inspection of the $(B/A)_n$ and $(C/A)_n$ flux-ratio curves shows changes of up to $\sim 40\%$ on time scales of

several months. Because the time delays between the cusp images are only a fraction of a day (Fassnacht et al. 1999b), residual intrinsic source variability can not cause these variations.

A more quantitative analysis based on the structure function (e.g. Simonetti et al. 1985) of the flux-ratio curves (indicated by $R(t)$) is shown in Fig.2. The structure function $\langle D^{(1)}(\tau) \rangle = \langle [R(t + \tau) - R(t)]^2 \rangle$ quantifies the average rms fluctuations (squared) between two points on the same flux-ratio curve, separated by a time lag τ . A lower value of $\langle D^{(1)}(\tau) \rangle$ means a stronger correlation (assuming no errors). Fig.2 shows that, even though $\langle D^{(1)}(\tau) \rangle$ fluctuates considerably, it continues to increase toward longer lags. Around $\tau \sim 150$ d, the rms suddenly decreases considerably, suggesting possible long-term correlated variations in the flux-ratios on that time-scale. If $\langle D^{(1)}(\tau) \rangle$ increases beyond $\tau \gtrsim 200$ days, flux-density variations of several tens of percent on a time-scale of $\gtrsim 1$ yr could be present as well. However, we note that the overlap of the flux-ratio curves becomes smaller for longer lags and consequently the errors become larger. Longer observations are required to make stronger statements about the longer time lags. Even so, similar fluctuations of the structure function are seen in other scintillating sources (e.g. Dennett-Thorpe & de Bruyn 2003).

Several reliability checks of the extrinsic variations of the cusp images of B2045+265 are called for: First we note that the lensed images are of roughly equal brightness and – within a factor about two – as bright as the images in B0128+437, B1359+154, B0712+472 and B1555+375. Hence there is no indication that the observed flux-ratio variations are related to the faintness or brightness of the lensed images. Second, there are no problems with the closeness between the cusp images ($\gtrsim 0.3''$) and the separation of their flux densities because of the high resolution of the MERLIN radio maps (~ 50 mas). Hence the fluxes of the three images are fully independent. Third, we have calculated the Spearman rank correlation coefficients (r_S) between each of its images A, B and C and those of the other five lens systems. This leads to 45 independent values of r_S (i.e. noise does not introduce correlation in this case), which on average should tend to zero. We find $\langle r_S \rangle = 0.0024$ and an rms of 0.153. The theoretical expectation value of the rms value is $1/\sqrt{N-1} = 0.151$, where $N = 45$ in our case. Hence, we recover the expectation values of both the average and rms. This shows that any correlation between the images can not be the result of obvious systematic errors in the data-reduction process, in the creation of the flux-ratio curves, or in our analysis.

Hence, we confidently conclude that the cusp images of B2045+265 show strong evidence for the presence of extrinsic variability.

4. Discussion & Conclusions

We have presented the flux-ratio curves of six gravitational lens systems, each composed of 41 epochs taken over a period of 8.5 months in 2001 with MERLIN at 5 GHz, as part of a MERLIN Key-Project. The systems were chosen to have merging cusp or fold images, such that the time-delays between these images are negligible ($\lesssim 1$ d) compared to the time-scale of intrinsic variability and the rate at which the light curves are sampled. The flux-ratio curves should therefore be void of intrinsic variability and multiplicative errors. The main goal of our program was to find additional cases of extrinsic variability other than radio-microlensing in B1600+434 (Koopmans & de Bruyn 2000, 2003).

We find some statistical evidence for extrinsic variability in all six lens systems, based on reduced χ^2_r values larger than unity (Sect.3.2; Tables 1 & 2). Residual intrinsic variations – due to the finite time delays – or small additive error are unlikely to be the cause of this, but can not fully be excluded yet. The high resolution of MERLIN also ensures negligible correlations between the fluxes of the merging images. The evidence for B0128+437, B1359+154, B1422+231 and B1555+375 is fairly marginal. The case for B0712 is stronger, however, and this object clearly deserves further study. The best case is B2045+265, which we discuss further below.

Even though radio-microlensing cannot be excluded, we think at this point that Galactic scintillation is the more likely cause of some of the higher values of χ^2 (Tables 1 & 2). Indeed, *all* compact extragalactic radio sources should show refractive scintillation at some level. At wavelengths of 5 GHz and for image sizes ~ 1 mas, the expected rms fluctuations due to scintillation, in a typical line-of-sight out of the Galactic plane, are a few percent (e.g. Walker 1998, 2001), which are comparable to the observed flux-density errors.

One gravitational lens systems, B2045+265, shows unambiguous evidence for extrinsic variability, based on the reduced χ^2 values significantly larger than unity (Tables 1 & 2) and visually apparent long-term variations in its flux-ratio curves (Fig.1). One possible explanation for the variations is radio microlensing similar to B1600+434 (Koopmans & de Bruyn 2000, 2003). However, because B2045+265 has a Galactic latitude $b \approx -10^\circ$ and is the lowest Galactic latitude system in our sample, Galactic refractive scintillation is the more likely explanation.

To examine this, first we naively use the revised electron-density model of our Galaxy by Cordes & Lazio (2003). This model gives a scattering measure of 8×10^{-4} kpc m $^{-20/3}$, an angular broadening at 5 GHz of 50 μ as and a transition frequency of 22 GHz between the weak and strong scattering regimes. If we choose the source size to be 250 μ as, we find a modulation index of 7% (from Walker 1998, 2001) or an rms scatter of $\sim 10\%$ in the flux-ratio

curves (as observed; Table 1), and a typical variability time-scale of ~ 1 week for an effective transverse velocity (i.e. the velocity of the ISM, earth, local and solar peculiar motions combined) of the medium of 50 km s^{-1} . Note however that the time-scale of variability might vary with time of the year due to the earth’s motion (e.g. Dennett-Thorpe & de Bruyn 2000, 2002).

Refractive scintillation could therefore explain the observed extrinsic variations up to a time-scale of possibly several weeks in B2045+265 for reasonable lensed-images sizes. However, the structure function shows correlated variations on time-scales that are much longer. These could either indicate modification(s) of the Kolmogorov spectrum of density fluctuations that was assumed in the above calculation or a very low transverse velocity of the medium, i.e. 10 km s^{-1} . If there is more power in the spectrum on larger scales, or a cutoff on smaller scales, fluctuations will become stronger on longer time scales (e.g. Blandford et al. 1986; Romani, Narayan & Blandford 1986; Goodman et al. 1987). Such large-scale electron density waves might also explain the apparent fluctuations in the observed structure function (Fig.2).

On further examination, however, we find that B2045+265 is very close, if not seen through, the Cygnus “superbubble” region (see Fig.6 in Fey, Spangler & Mutel 1989), making our analysis based on the model in Cordes & Lazio (2003) rather uncertain. This region has considerably enhanced scattering measures and if this is the case for B2045+265 as well, it would strongly support Galactic scintillation as the cause of the observed flux-density variations. The complexity of such regions, where turbulence in the ionized ISM presumably originates, could be the reason why we see large-amplitude fluctuations in the flux ratios with time scales that are not expected from simple Kolmogorov turbulence models (see also e.g. J1819+3845; Dennett-Thorpe & de Bruyn 2000, 2002).

Finally, it is interesting to note that B2045+265 has the strongest and most significant violation of the cusp relation of all known lens systems (Keeton et al. 2003). Even so, the values of R_{cusp} of the systems discussed in this paper (see Table 1) agree with those in Keeton et al. (2003). However, the strong observed variations in the flux-ratio curves should caution against the use of both flux-ratios and values of R_{cusp} (Sect.1) – derived from single-epoch observations – even if the inferred time-delays are only a few hours!

Whether the violation of the cusp relation in B2045+265, averaged over 8.5 months (Table 1), and Galactic refractive scintillation and/or scattering is completely coincidental, is not clear at this point. At any instant in time, however, large scale electron-density fluctuations in the Galactic ISM can focus or defocus the images with long time scales of variability – as is apparent from our observations – probably even more so toward regions of enhanced turbulence (i.e. the Cygnus region). CDM substructure mostly focuses the images.

It is interesting to note that B0712+472, probably the system with second-best evidence for extrinsic variability in our sample, also has a low Galactic latitude $b = +23^\circ$.

While the observations reported in this paper do not contradict the exciting conclusion that CDM substructure might have been detected within the central regions of lens galaxies, they do suggest that extrinsic, refractive effects are also of importance and that it is imperative to carry out further, multi-frequency monitoring to distinguish them from achromatic, gravitational effects.

LVEK acknowledges the support from an STScI Fellowship grant. RDB is supported by an NSF grant AST-0206286. MERLIN is a National Facility operated by the University of Manchester at Jodrell Bank Observatory on behalf of PPARC. LVEK thanks Chris Kochanek and Neal Dalal for suggestions that improved the presentation of this work. We thank the referee for helping to clarify the manuscript.

REFERENCES

Biggs, A., et al., 2003, in preparation

Blandford, R., Narayan, R., & Romani, R. W. 1986, *ApJ*, 301, L53

Blandford, R. D. 1990, *QJRAS*, 31, 305

Bradač, M., Schneider, P., Steinmetz, M., Lombardi, M., King, L. J., & Porcas, R. 2002, *A&A*, 388, 373

Burud, I. et al. 2000, *ApJ*, 544, 117

Chiba, M. 2002, *ApJ*, 565, 17

Cordes, J. M. & Lazio, T. J. W., 2003, [astro-ph/0207156]

Dalal, N. & Kochanek, C. S. 2002, *ApJ*, 572, 25

Dennett-Thorpe, J. & de Bruyn, A. G. 2000, *ApJ*, 529, L65

Dennett-Thorpe, J. & de Bruyn, A. G. 2002, *Nature*, 415, 57

Dennett-Thorpe, J. & de Bruyn, A. G. 2003, *A&A*, accepted, [astro-ph/0303201]

Fassnacht, C. D., Pearson, T. J., Readhead, A. C. S., Browne, I. W. A., Koopmans, L. V. E., Myers, S. T., & Wilkinson, P. N. 1999a, *ApJ*, 527, 498

Fassnacht, C. D. et al. 1999b, AJ, 117, 658

Fassnacht, C. D., Xanthopoulos, E., Koopmans, L. V. E., & Rusin, D. 2002, ApJ, 581, 823

Fey, A. L., Spangler, S. R., & Mutel, R. L. 1989, ApJ, 337, 730

Goodman, J. J., Romani, R. W., Blandford, R. D., & Narayan, R. 1987, MNRAS, 229, 73

Keeping, E. S., 1962, *Introduction to statistical inference*, Princeton, N.J, Van Nostrand

Keeton, C. R., 2001, submitted to ApJ, [astro-ph/0111595]

Keeton, C. R., Gaudi, B. S., & Petters, A. O., 2003, submitted to ApJ, [astro-ph/0210318]

Klypin, A., Kravtsov, A. V., Valenzuela, O., & Prada, F. 1999, ApJ, 522, 82

Kochanek, C. S. & Dalal, N. 2003, submitted to ApJ, [astro-ph/0302036]

Koopmans, L. V. E., de Bruyn, A. G., Xanthopoulos, E., & Fassnacht, C. D. 2000, A&A, 356, 391

Koopmans, L. V. E. & de Bruyn, A. G. 2000, A&A, 358, 793

Koopmans, L. V. E. & de Bruyn, A. G. 2003, in preparation

Mao, S. & Schneider, P. 1998, MNRAS, 295, 587

Metcalf, R. B. & Madau, P. 2001, ApJ, 563, 9

Metcalf, R. B. & Zhao, H. 2002, ApJ, 567, L5

Moore, B., Ghigna, S., Governato, F., Lake, G., Quinn, T., Stadel, J., & Tozzi, P. 1999, ApJ, 524, L19

Romani, R. W., Narayan, R., & Blandford, R. 1986, MNRAS, 220, 19

Schechter, P. L. & Wambsganss, J. 2002, ApJ, 580, 685

Schneider, P. & Weiss, A. 1992, A&A, 260, 1

Simonetti, J. H., Cordes, J. M., & Heeschen, D. S. 1985, ApJ, 296, 46

Walker, M. A. 1998, MNRAS, 294, 307

Walker, M. A. 2001, MNRAS, 321, 176

	$\langle r_{(B/A)} \rangle$	$\langle r_{(C/A)} \rangle$	$\langle r_{(D/A)} \rangle$	χ^2/DOF	R_{cusp} (ABC)
B0128+437	0.584(0.029)	0.520(0.029)	0.506(0.032)	1.8/1.9/2.4	0.445 (0.018)
B0712+472	0.843(0.061)	0.418(0.037)	0.082(0.035)	4.8/3.2/8.0	0.255 (0.030)
B1359+154	0.580(0.039)	0.782(0.031)	0.193(0.031)	1.9/0.9/1.2	0.510 (0.024)
B1422+231	1.062(0.009)	0.551(0.007)	0.024(0.006)	1.8/2.0/1.5	0.187 (0.004)
B1555+375	0.620(0.039)	0.507(0.030)	0.086(0.024)	3.4/2.1/2.4	0.417 (0.024)
B2045+265	0.578(0.059)	0.739(0.073)	0.102(0.025)	8.2/10.9/2.9	0.501 (0.035)

Table 1.— The flux-ratios of each image pair. The rms scatter in the flux-ratio is indicated between parentheses, calculated from the 41 epochs. The reduced χ^2 values are listed as well, calculated on the basis that each normalized flux-ratio curve should be unity and that there is no variability. In addition, the values of R_{cusp} (see Sect.1) and its rms (between parentheses) are listed (e.g. Mao & Schneider 1998; Keeton et al. 2002).

	rms(a_{ext})	rms(b_{ext})	rms(c_{ext})	χ_r^2/DOF
B0128+437	2.9%	1.9%	2.5%	3.3
B0712+472	4.8%	4.2%	4.8%	6.2
B1359+154	1.0%	4.6%	—	2.8
B1422+231	—	0.6%	0.9%	3.7
B1555+375	3.3%	4.2%	3.0%	5.3
B2045+265	6.1%	7.0%	7.2%	17.1

Table 2.— The estimated rms levels of extrinsic variability in images A, B and C. The reduced values of χ_r^2 are given to indicate the significance of the presence of extrinsic variability in the combined set of images. The dashes indicate that the estimated variance was smaller than zero (see Sect.3.2 for more details).

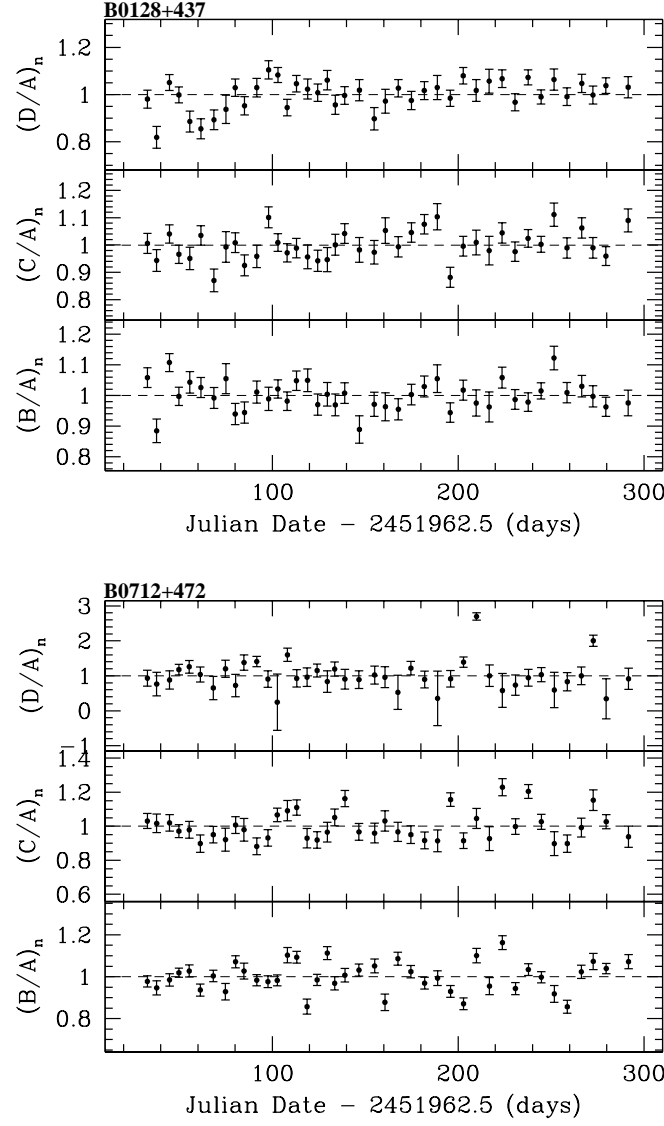


Fig. 1.— The normalized flux-ratio curves of the three independent image pairs for all six quadrupole lens systems. The scale on the y-axis is set to ± 5 times the rms scatter of the flux-ratio curves. The errors on the flux-ratio curves are determined from the errors on the individual flux-density curves.

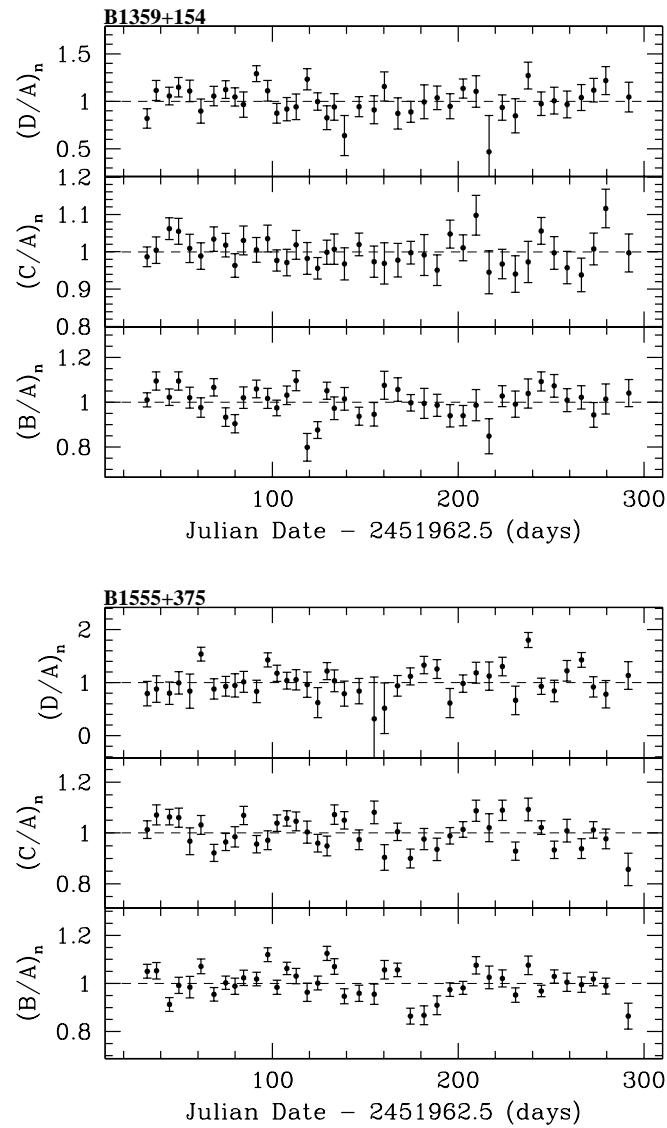


Fig. 1.— Continued

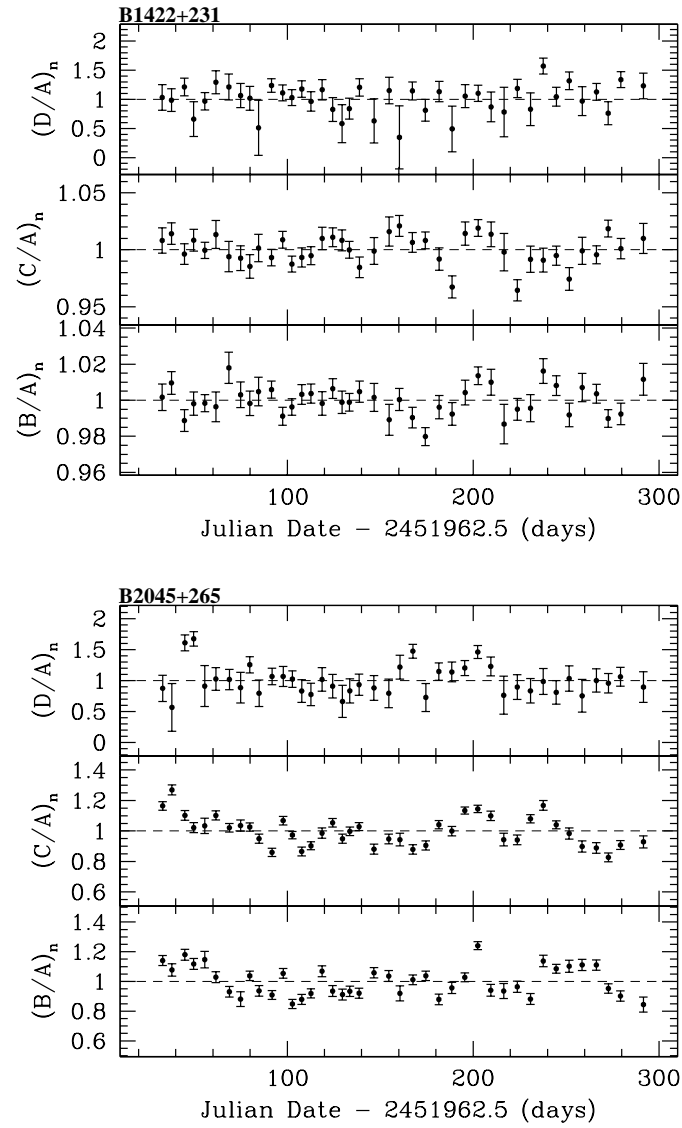


Fig. 1.— Continued

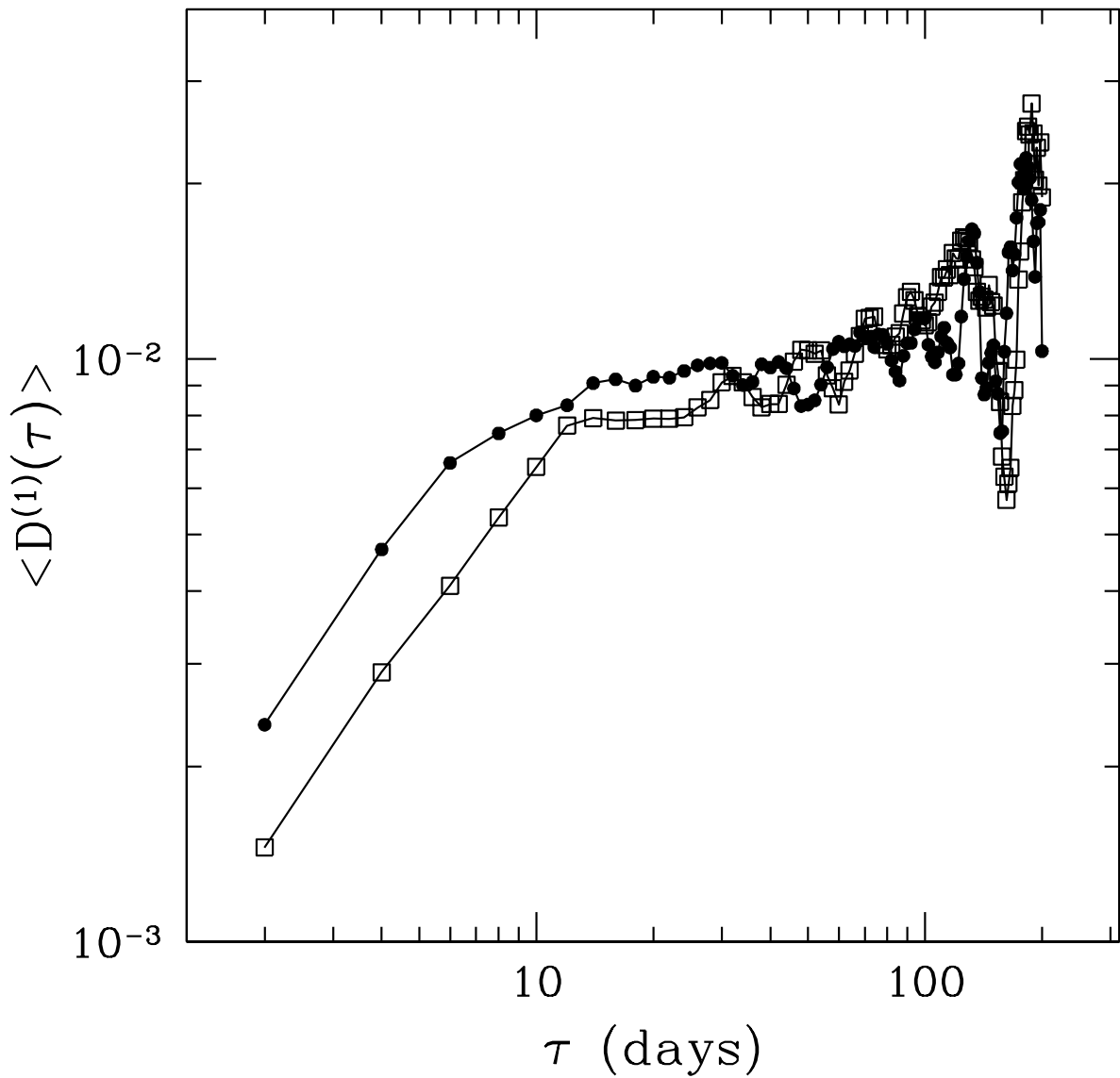


Fig. 2.— The structure functions of the normalized flux-ratio curves $(B/A)_n$ (circles) and $(C/A)_n$ (open squares) of B2045+265 between time-lags of 2 and 200 days. The break below ~ 10 d is the result of variations in the flux-ratio curves that correlate on that time scale, but are also affected by the on-average 1-week time separation between observations.